Observing convective activities in complex convective organizations and their contributions to precipitation and anvil cloud amounts

Zhenquan Wang[1, *], Jian Yuan[1]

[1] School of Atmospheric Sciences, Nanjing University, Nanjing, China

Correspondence to: Zhenquan Wang (zhqwang@smail.nju.edu.cn)

Abstract. The convective processes of precipitation and the production of anvil clouds determine the Earth's water and radiative budgets. However, convection could have very complicated convective organizations and behaviors in the tropics. Many convective activities in various life stages are connected in complex convective organizations, and it is difficult to distinguish their behaviors. In this work, on the basis of hourly infrared brightness temperature (BT) satellite images, with a novel variable-BT tracking algorithm, complex convective organizations are partitioned into organization segments of single cold cores as tracking targets. The detailed evolution of the organization structures (e.g., the variation in the cold-core BT, mergers and splits of cold cores) can be tracked, and precipitation and anvil clouds are explicitly associated with unique cold cores. Compared with previous tracking algorithms that focused only on variations in areas, the novel variable-BT tracking algorithm is capable of documenting the evolution of both the area and BT structures. For validation, the tracked motions are compared against the radiosonde cloud-top winds, with mean speed differences of -1.6 m/s and mean angle differences of 0.5°.

With the novel variable-BT tracking algorithm, the behaviors of oceanic convection over the tropical western Pacific Ocean are investigated. The results show that the duration, precipitation and anvil amount of the lifecycle accumulation all have simple loglinear relationships with the cold-core-peak BT. The organization segments of the peak BT values less than 220 K are long-lived, with average durations of 4-16 hours, whereas the organization segments of the warmer-peak BT values disappear rapidly within a few hours but with a high occurrence frequency. The decay process after the cold core peaks contributes to more precipitation and anvil clouds than does the development process. With the core peaking at a colder BT, the differences in the accumulated duration, precipitation and anvil production between the development and decay stages increase exponentially. Additionally, the occurrence frequency of mergers and splits also has a loglinear relationship with the cold-core-peak BT. For the lifecycles of the same cold-core-peak BT, the lifetime-accumulated precipitation and anvil amount are strongly enhanced in complicated lifecycles with the occurrence of mergers and splits compared with those with no mergers or splits. For the total tropical convective cloud water budget, long-lived complicated lifecycles make the largest contribution to precipitation, whereas long-lived complicated and short-lived simple lifecycles make comparable contributions to the anvil cloud amount and are both important.

1. Introduction

Precipitation and anvil clouds are two key components of the convective cloud water budget but are usually accompanied by very complicated microphysical and dynamic processes. In climate models, their representations are determined by tunable parameters with large uncertainties, e.g., detrainment and precipitation efficiency (Rennó et al., 1994; Zhao, 2014; Clement and Soden, 2005; Zhao et al., 2016; Suzuki et al., 2013). In cloud-resolving models, the parameterization scheme of convection is still subject to many uncertainties in ice microphysics and subgrid turbulence (Matsui et al., 2009; Blossey et al., 2007; Powell et al., 2012; Bretherton, 2015; Atlas et al., 2024), although cloud dynamics and microphysics can be resolved at fine scales. The challenge is partially because the detailed convection processes of precipitation and the production of anvil clouds have not been sufficiently explored from observations to advance understanding and model parameterization.

The spatial organization of convection varies from a simple isolated cell to a complicated structure that consists of many

convective activities in various life stages. The variation in convection organizations is closely related to changes in precipitation and the anvil cloud amount (Yuan and Houze, 2010; Yuan et al., 2011; Tobin et al., 2012; Wing and Emanuel, 2014; Mauritsen and Stevens, 2015; Ruppert and Hohenegger, 2018; Bony et al., 2020; Bao and Sherwood, 2019; Houze, 2004). Cloud-resolving models and observations both suggest that convective organizations are important bridges for the interactions between convection and the environment (Tobin et al., 2012; Blossey et al., 2005; Coppin and Bony, 2015; Wing and Emanuel, 2014; Wing et al., 2017; Holloway et al., 2017; Muller and Bony, 2015; Sokol and Hartmann, 2022). Through radiative feedback and circulation, convective organizations are associated with the nonconvecting environment. The drier free troposphere and enhanced radiative cooling of the nonconvecting regions can reinforce subsidence to expand the dry region and thereby force the convection in the moist region to aggregate (Blossey et al., 2005; Coppin and Bony, 2015). Over warm oceans, stronger mass convergence and surface turbulent fluxes promote aggregation by developing deep convection and inhibiting scattered convective activities (Coppin and Bony, 2015; Holloway et al., 2017; Wing et al., 2017). Although organizational variations can influence precipitation efficiency (Bao and Sherwood, 2019), when the total atmospheric water amount is not known and is difficult to measure, increased precipitation efficiency does not guarantee a decrease in the anvil cloud amount. Thus, the links among convective organizations, precipitation and anvil clouds still need further observational evidence as constraints for understanding their climate feedback processes.

However, observing the organization and behavior of convection is still challenging. Although active radar and lidar sensors on polar-orbit satellites and ground-based observatories can penetrate convective clouds, their spatiotemporal sampling is too sparse for tracking. From the images of the brightness temperature at 10.8 μm (BT_{11}) of geostationary satellites (GEOs), pixels of thin cirrus clouds cannot be accurately distinguished from cloudless pixels, but the major structure of the organized convection, consisting of the deep convective clouds and the associated anvil clouds, can be observed continuously in time and used for tracking (Richards and Arkin, 1981; Hendon and Woodberry, 1993; Fu et al., 1990). For the identification of convection from GEO images, two methods have been proposed in previous studies. One method is to identify the contiguous area under a fixed BT_{11} threshold (Goyens et al., 2011; Schröder et al., 2009; Huang et al., 2018; Williams and Houze, 1987; Chen and Houze, 1997; Kolios and Feidas, 2009; Laing et al., 2008; Feidas and Cartalis, 2007; Fu et al., 2023; Yang et al., 2020; Tsakraklides and Evans, 2003). On the basis of the fixed threshold, the identified targets are usually of complex organizations and it is not capable of being used to distinguish the detailed convective activities inside complex organizations. In addition, variable-BT_{11} identification has been proposed in recent years, in which a set of adaptive BT_{11} thresholds are used to divide the clustered convection complex into independent convective systems for tracking (Yuan and Houze, 2010; Fiolleau and Roca, 2013; Feng et al., 2023; De Laat et al., 2017; Bouniol et al., 2016; Heikenfeld et al., 2019; Zinner et al., 2008; Zinner et al., 2013). This approach makes it possible to track the detailed variations in complex convection organizations, particularly with respect to tracking the evolution of the BT_{11} structures.

Convective systems can merge and split and their BT_{11} structures can change rapidly. These complicated behaviors make them difficult to track. The most widely used tracking method is based on the overlap in areas between two targets at different times (Williams and Houze, 1987). This method permits mergers and splits but has flaws in tracking fast-moving clouds (Huang et al., 2018). On the other hand, cloud movements can be well derived via cross correlation to match the cloud BT_{11} patterns at different times (Leese et al., 1971; Nieman et al., 1997; Velden et al., 1998; Salonen and Bormann, 2016; Hersbach et al., 2020). Thus, these two methods are complementary and can be combined to first derive cloud displacements and then determine the temporal associations between targets according to the dynamic overlap (i.e., the overlap in areas after movement) (Feng et al., 2023; Zinner et al., 2013).

In this work, complex convective organizations (CCOs) are segmented into simple structural components of single cold cores and tracked separately according to variable-BT_{11} identification and dynamic overlap. Compared with fixed-threshold tracking, the variable-BT_{11} tracking algorithm has the advantages of documenting more detailed convective evolution in CCOs. Although several variable-BT_{11} tracking algorithms have been proposed, the tracked lifecycle is still described mostly by the

variation in areas and lacks of the BT_{11} structural information. By the novel variable-BT_{11} tracking algorithm developed in this work, the tracked lifecycle is described by the cold-core BT_{11} variation in the CCO structural components. The precipitation and non-precipitating anvil clouds are explicitly associated with unique cold cores.

This paper is laid out as follows: Sect. 2 describes the data and methods used in our analyses. Sect. 3 introduces the novel variable-BT_{11} segment tracking algorithm and its comparison to fixed-threshold tracking. Sect. 4 explores the relationships of the convective duration, precipitation and anvil production with the BT_{11} structures. Sect. 5 presents conclusions.

2. Data and methods

2.1 Images from GEOs

The BT_{11} in the tropics between 20°S-20°N and 90°W-170°E was scanned by radiometer imagers on geostationary Multi-functional Transport Satellite 1 Replacement and 2 Replacement (MTSAT-1R and -2R), with a scanning start time of half an hour and view zenith angles of less than 60°. The BT_{11} images from 2006 with 1-hour and 8-km resolution were obtained from the Satellite ClOud and Radiative Property retrieval System (SatCORPS) of the Clouds and the Earth's Radiant Energy System (CERES) project. In the CERES SatCORPS, the BT_{11} was calibrated against the Moderate Resolution Imaging Spectroradiometer (MODIS) from the Aqua (Doelling et al., 2013; Doelling et al., 2016). To facilitate data processing, the BT_{11} images of 8-km pixels were further gridded to 0.05° via linear interpolation (Amidror, 2002).

2.2 Global precipitation measurement (GPM)

At fine scales (0.1° and half-hour resolution), the GPM data combines all available sensors for precipitation estimates, including microwave imagers from multiple low-Earth orbit satellites, the infrared (IR) channel of GEO radiometers and land-surface rain gauges (Huffman et al., 2007; Huffman et al., 1997). The microwave brightness temperature is sensitive to atmospheric hydrometers of precipitation but has sparse spatiotemporal sampling due to its sun-synchronous orbit. For grids without microwave observations, the GEO-IR BT_{11} was used to estimate precipitation according to the spatially varying calibration coefficient of the microwave precipitation rates (Huffman et al., 1997). To improve accuracy, rain gauges were further used to rescale satellite estimates of precipitation rates (Huffman et al., 1997). It has been demonstrated that this satellite-based precipitation product performs well for strong precipitation events with a mean bias smaller than 1 mm/day but misses 20-80% of the light precipitation (< 10 mm/day) (Tian et al., 2009). In the tropics, light precipitation (< 1 mm/hour) accounts for approximately 55-70% of the precipitation area but contributes to only 9-18% of the total precipitation (Yuan and Houze, 2010). Only precipitation rates greater than 1 mm/hour are considered the regions with precipitation in this work since light precipitation has high uncertainty in the GPM data and relatively low contributions to total precipitation.

2.3 Cloud-top winds from ground-based radar and radiosonde observations

Cloud detection from radar and wind observations from radiosondes were combined to derive cloud-top winds at three tropical ground-based observatories of the Atmospheric Radiation Measurement (ARM) program: Darwin (130.9°E, 12.4°S), Manus Island (147.4°E, 2.1°S) and Nauru Island (166.9°E, 0.5°S). The vertical distribution of hydrometers up to 20 km above the ground was detected via 35 GHz millimeter-wave cloud radar (MMCR), with temporal and spatial resolution of 10 s and 45 m, respectively. The best estimate reflectivity of the MMCR in the range of -50 to 20 dBZ was provided in the ARM program Active Remote Sensing of Clouds (ARSCL) value-added product at the three sites. A reflectivity higher than -40 dBZ was identified as a cloud (Zhao et al., 2017). To match the GEO observations, the instantaneous cloud profiles within 5 minutes around the time of the GEO radiometer imager scanning at these three sites were collected to compute the cloud fraction. The 10-min cloud-fraction profile was computed as the ratio of the number of cloud occurrences to the total number of observations at each height. Continuous levels of the cloud fraction greater than zero were identified as cloud layers. The thickest high cloud layer with a top greater than 5 km and a maximum cloud fraction of at least 50% was selected as the major high cloud layer passing over the sites. The cloud top refers to the uppermost height of the major cloud layer.

Winds were detected by the ARM balloon-borne radiosondes with high vertical and temporal resolutions of 10 m and 2.5 s, respectively. The accuracy of the radiosonde wind speed was approximately 0.5 m/s. The radiosondes were launched two times a day at Manus and Nauru (approximately 11:30 and 23:30 UTC) and four times a day at Darwin (approximately 4:30, 11:15, 16:30 and 23:15 UTC). Compared with the instantaneous cloud detection of the MMCR, balloon-borne radiosondes might take hours and drift dozens of kilometers away from the launch location to approach the cloud top height. To collocate the cloud and wind observations, the time difference between the balloon-borne radiosondes reaching the cloud top and the MMCR observations of the cloud top must be within one hour for quality control.

2.4 Comparison of cloud-top winds and tracked cloud motions

The difference between the observed cloud-top winds and the tracked cloud motions is assessed as follows, which is consistent with those in Nieman et al. (1997):

$$Speed\ bias = \frac{1}{N}\sum_{i=1}^{N}\left(\sqrt{U_i^2 + V_i^2} - \sqrt{U_r^2 + V_r^2}\right), \quad (1)$$

$$Angle\ bias = \frac{1}{N}\sum_{i=1}^{N}(\arctan\left(\frac{V_i}{U_i}\right) - \arctan\left(\frac{V_r}{U_r}\right)), \quad (2)$$

$$MVD = \frac{1}{N}\sum_{i=1}^{N}\sqrt{(U_i - U_r)^2 + (V_i - V_r)^2}, \quad (3)$$

$$SD = \sqrt{\frac{1}{N}\sum_{i=1}^{N}(\sqrt{(U_i - U_r)^2 + (V_i - V_r)^2} - MVD)^2}, \quad (4)$$

$$RMSE = \sqrt{MVD^2 + SD^2}. \quad (5)$$

Here, the mean speed and angle bias, the mean vector difference (MVD), the standard deviation (SD) of the MVD and the root-mean-square error (RMSE) of the tracked cloud motions compared with the observational cloud-top winds were computed. U and V are the x- and y-component winds, respectively. The subscripts i and r indicate an individual sample of the tracked cloud motion and the corresponding reference cloud-top winds of radiosondes, respectively, and N is the total number of samples.

2.5 *t* test and confidence intervals

The 95% confidence interval for the mean value was computed via the t test: $\bar{x} \pm t_c \frac{s}{\sqrt{N}}$, where $\bar{x}$ is the mean value of all samples; t_c is the critical value for t; and s is the standard deviation of all the samples. N is the number of independent samples, and N is determined by the sample length divided by the distance between independent samples (Bretherton et al., 1999).

3. Tracking the convective organization segments

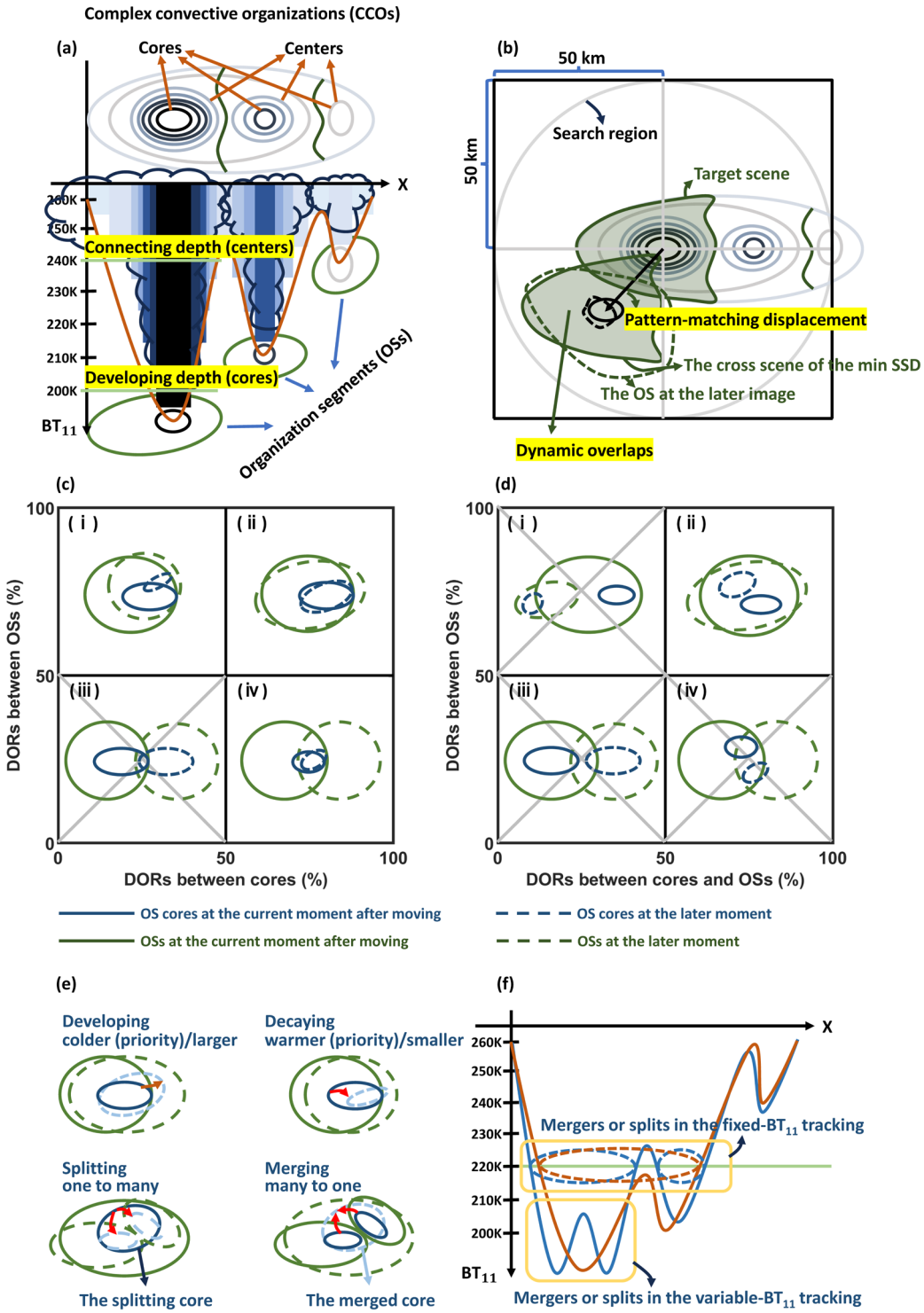

Figure 1. Illustrations of the variable-BT_{11} segment tracking algorithm. (a) Example illustrations of segmenting the CCO into single-core OSs as tracking targets. The CCO 3-dimensional structures in x, y and BT_{11} are identified by the adaptive variable-BT_{11} thresholds. The cold-core BT_{11} indicates the depth of development. The cold-center BT_{11} indicates the depth of the connection. (b) Example illustrations of tracking the OS by combining cross correlation and the overlap in areas. The OS is moved according to the displacement predicted by cross correlation and then overlaps with the OSs in the later images. (c-d) The dynamic overlapping situations of two OSs of different moments when their cores have overlaps and no overlaps, respectively. The solid blue and green lines indicate the OS core and segmentation outlines of the current moment at the location predicted by cross correlation, respectively. The dashed blue and green lines indicate the OS core and segmentation outlines of the later moment, respectively. The gray cross indicates the non-association between OSs. (e) Examples illustrating tracked OS evolution (i.e., development, decay, mergers and splits). The red arrows indicate the evolution of the OS with time. (f) Illustrations of the difference between the variable-BT_{11} and fixed-BT_{11} tracking for mergers and splits. The solid red and blue lines are the CCO BT_{11} structures at different times captured by the adaptive variable-BT_{11} thresholds. The dashed red and blue contours are the mergers and splits captured by the fixed threshold of 220 K.

To distinguish the behaviors of clustered convective activities in CCOs, the organization segments (OSs) of single but variable-BT_{11} cold cores (Fig. 1a) are partitioned as tracking targets and are tracked by combining the cross correlation and the area overlap (Fig. 1b) based on the hourly infrared satellite images. This novel variable-BT_{11} segment tracking algorithm and its difference from the conventional fixed-threshold tracking algorithm are introduced in this section as follows.

(1) Segmenting CCOs into the OSs of single cold cores

As illustrated in Fig. 1a, the CCO is the complex organization of multiple connected convections and is identified as the contiguous area of the BT_{11} that is colder than 260 K. The 260-K threshold can enclose 95% of deep convective clouds and as much of the anvil cloud as possible but with the least contamination from lower-level clouds (Yuan and Houze, 2010; Yuan et al., 2011; Chen and Houze, 1997). The segmented single-core structural component of CCOs is identified as the OS to be used as the tracking target. A set of adaptively variable-BT_{11} thresholds from 180-260 K per 5-K interval and a minimum area threshold of 1000 km^2 are used to capture the "growth rings" in CCOs. In Fig. 1a, these rings reflect the CCO structure in three dimensions, namely x, y and BT_{11}, and are the fundamental indicators of internal dynamics (Houze, 2004). The innermost ring of the coldest local BT_{11} is defined as the cold core, which is the most active vertically developing region in the OS. The BT_{11} of the cold core represents the depth at which the OS developed. For a CCO consisting of multiple cold cores, the BT_{11} of the coldest core in the CCO is defined as the CCO BT_{11} for representing the depth of CCO development. The isolated ring of the warmest BT_{11} and enclosing only one core is the cold center. The OS would be connected (disconnected) to the surrounding OSs outside (inside) the center. Thus the cold-center BT_{11} can be used to indicate the connecting condition between the OSs in the CCO.

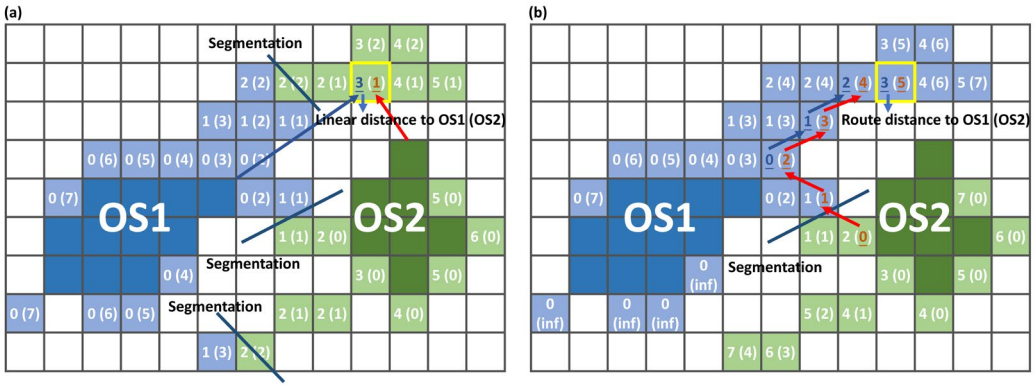

Figure 2. Illustrations of segmentation according to the nearest linear distance (a) and the nearest route distance (b). The dark blue and green pixels represent the OS1 and OS2 centers, respectively. The colored pixels outside the centers are the pixels to be assigned in the contour of the cold-center BT_{11} plus 1 K. The light blue and green pixels are assigned to OS1 and OS2, respectively. The numbers inside those pixels indicate the number of necessary pixels to connect with OS1 and OS2, respectively. The arrows in (a) and (b) represent the nearest distances of OS1 and OS2 to reach the yellow-edge pixel, as examples to illustrate the computations of the linear distance and the route distance, respectively.

For segmentation, the pixels lying outside the centers are assigned to the connected neighborhood OSs by the 1-K interval. To be specific, all BT_{11} contours of the 1-K interval between the cold-center BT_{11} and 260 K need to be found first. The assignment of the pixels outside the centers is conducted in the order from cold to warm BT_{11} contours of the 1-K interval. The initial OS is just the center and it is updated after every 1-K-interval assignment. An example illustration of the 1-K-interval assignment is shown in Fig. 2. On the basis of the 8-point-connected neighborhood in which the 8 surrounding points are recognized as the connected neighborhood to the center point, the distance between two pixels is computed as the number of necessary pixels connecting them. According to the nearest linear distance, as shown in Fig. 2a, some of the pixels assigned to OS2 (those light green pixels in Fig. 2a) are disconnected from OS2 but connected to OS1. After the assignment, OS2 is composed of two disconnected parts. For an organized convective system, the assigned pixels outside the center can also be understood as outflowing anvil clouds from the center. It would be strange that the outflowing anvil clouds from OS2 are not connected with its original OS2 but connected with OS1. To avoid these conditions, the distance of the nearest route is used to determine the pixel assignment. Here, the route of OS1 and OS2 to reach a pixel (the blue and red arrows in Fig. 2b) is confined

to within the 1-K-interval contour. Pixels of the same distance to OS1 and OS2 are randomly assigned. In Fig. 2b, the assignment of the pixels on the basis of the distance of the nearest route is more reasonable than that in Fig. 2a on the basis of the nearest linear distance. Thus, in every 1-K-interval assignment, the distance of the nearest route is used to accomplish the segmentation and the OSs are updated with these newly assigned pixels iteratively until all the pixels within the CCO are assigned.

The final OS is the 3-dimensional (x, y and BT_{11}) structure of a single cold core. The OS can be further separated into precipitating and non-precipitating (precipitation less than 1 mm/hour) regions on the basis of the GPM. The non-precipitating area is identified as the anvil cloud. By segmentation, those precipitation and anvil pixels are explicitly associated with unique cold cores. The key definitions of variable-BT_{11} tracking are depicted in Fig. 1a and summarized in Table 1 for easy checking.

Table 1. Summary of the key definitions for variable-BT_{11} tracking developed in this study

Name	Definition
Complex convective organizations (CCOs)	The contiguous area of the BT_{11} colder than 260 K.
Organization segments (OSs)	The segmented single-core structural component of CCOs.
Cold-core BT_{11} (OS developing depth)	The local coldest BT_{11} contour in OSs.
Cold-center BT_{11} (OS connecting depth)	The local warmest isolated BT_{11} contour of only enclosing one core in OSs.
CCO BT_{11} (CCO developing depth)	The coldest cold-core BT_{11} of multiple cores in the CCO.
Anvil cloud	The non-precipitating (precipitation less than 1 mm/hour) region of each OS.
Dynamic overlapping rates (DORs)	The OS is moved to the location predicted by cross correlation and then overlaps with the OSs in the later image.
Merger and split BT_{11}	The BT_{11} of the merged cold core and the BT_{11} of the splitting cold core.
Cold-core-peak BT_{11}	The coldest cold-core BT_{11} in lifecycles, representing the convective peaking strength.
Development and decay stages	The stage before and after the time of the cold core peaking at the coldest BT_{11} (if there are multiple cores of the same BT_{11}, the one of the largest core areas is selected).
Lifecycle-accumulated duration, precipitation and anvil cloud amount	The accumulated time, precipitation and anvil cloud amount in the lifecycle.

(2) Tracking the displacement of OSs on the basis of cross correlation

The OS displacement is derived by searching for the maximum similarity of its BT_{11} pattern in the later image on the basis of the cross correlation (Leese et al., 1971; Velden et al., 1998). As shown in Fig. 1b, the target scene is the OS BT_{11} pattern. The search region is centered at the core centroid of the target and confined to a radius of 50 km, which corresponds to a maximum OS motion of 50 km/hour (Merrill et al., 1991). The cross scene has the same shape as the OS target and refers to all possible scenes to match the OS target within the search region. The BT_{11} pattern of the target scene is normalized, and so is the BT_{11} pattern of each cross scene. The patten-matching displacement is determined by the minimum of the sum of squared differences (SSD) of the normalized BT_{11} between the OS target scene and the cross scene:

$$SSD = \sum_{x,y}[BT'_{11}(x,y) - \widetilde{BT}'_{11}(x,y)]^2, \quad (6)$$

where $BT'_{11}(x,y)$ and $\widetilde{BT}'_{11}(x,y)$ are the normalized BT_{11} values at pixel (x, y) of the target scene and the cross scene in the search, respectively. Here, the minimum SSD corresponds to the maximum pattern correlation. The final match is examined by the pattern correlation coefficient. For the OS of areas larger (smaller) than 5000 km^2, the match is valid when the correlation of the pattern is greater than 0.6 (0.8). The correlation threshold values are consistent with those in Daniels et al. (2020).

Otherwise, the OS BT_{11} structures would change rapidly in one hour and would rather be considered stationary.

(3) Tracking OSs via dynamic overlaps

In Fig. 1b, to track the temporal evolution of OSs, the OS is moved to the location predicted by cross correlation and then overlaps with the OSs in the later image. In this way, the dynamic overlaps can be used to tolerate the fast-moving OS in tracking. For the OS with the core structure, three indices of the dynamic overlapping ratio (DOR) are considered to determine the associations of two OSs at different times for the same object, including the DOR between cores, the DOR between OSs and the DOR between cores and OSs. The DOR between cores is the ratio of their overlaps in cores relative to the minimum area of the cores to represent the degree of core overlap. The DOR between OSs is the ratio of the OS overlap relative to the minimum area of the OS to represent the degree of OS overlap. The DOR between cores and OSs is the ratio of the overlap of the OS to the core relative to the core area, representing the degree of the core overlapped by the later or previous OS.

Two OSs of different moments are associated in time and considered the same object when these two OSs overlap sufficiently. The overlapping situations of two OSs are distinguished by whether their cores overlap with each other (Fig. 1c) or not (Fig. 1d). Those pairs of OSs in situations (i), (ii) and (iv) in Fig. 1b all sufficiently overlap with the DOR between either cores or OSs greater than 50% and thus are associated in time to reflect the OS evolution with time. The situation (iii) in Fig. 1c with DORs of both cores and OSs less than 50% indicates that these two OSs have no associations. In Fig. 1d, when the cores of two OSs do not overlap, the determinant of the OS association relies on the DOR between OSs and the DOR of OSs to cores. In those cases, the OSs are associated in time only in situation (ii) in Fig. 1d, with those two DOR indices both larger than 50%. Those pairs of OSs in the other situations in Fig. 1d are obviously not associated. Overall, if the DORs of two OSs satisfy the overlapping conditions of (i), (ii) and (iv) in Fig. 1c and (ii) in Fig. 1d, they are associated in time.

For two temporally associated OSs, the development and decay can be inferred from the variation in the cold-core BT_{11} and area, as shown in Fig. 1e. The variation in the cold-core BT_{11} is prior to the variation in the cold-core areas for determining development and decay. If the cold-core BT_{11} is colder with time, or if the cold-core BT_{11} is the same but the cold-core area is larger with time, the OS is developing; otherwise, it decays. Notably, OSs are not necessarily associated with only one OS. As shown in Fig. 1e, mergers and splits are allowed in dynamic overlaps and are identified as the many-to-one and one-to-many OS associations, respectively. The merged cold-core BT_{11} and the splitting cold-core BT_{11} are documented as BT_{11} of mergers and splits, respectively.

In comparison, conventional fixed-threshold tracking infers development and decay from the variation in the area, which might involve multiple convective activities at different life stages. However, the variable-BT_{11} tracking infers the development and decay of each OS from the variation in both the cold-core BT_{11} and the area. Additionally, mergers and splits in fixed-threshold tracking are dependent on the selection of the BT_{11} threshold. Owing to the selection of the fixed BT_{11} threshold, the identified targets are usually connected under a warmer threshold but are disconnected under a colder threshold. As illustrated in Fig. 1f, if under the fixed threshold of 260 K, no mergers or splits occur. If under the fixed threshold of 220 K, the cutoff of the CCO by 220 K is the connected complex of multiple cores or two disconnected parts at different times. This change in the connecting conditions over time under the selected fixed threshold results in mergers and splits in fixed-threshold tracking. If under the fixed threshold of 200 K, the mergers and splits of cold cores are captured. It manifests that mergers and splits in fixed-threshold tracking can be attributed to many reasons: the threshold selection, the change in the connecting conditions and the variation in cold cores over time. In contrast, in variable-BT_{11} tracking, mergers and splits are not influenced by changes in the connecting conditions over time but is only related to the variation in cold cores as illustrated in Fig. 1e-f.

(4) Quality control and validation of variable-BT_{11} segment tracking

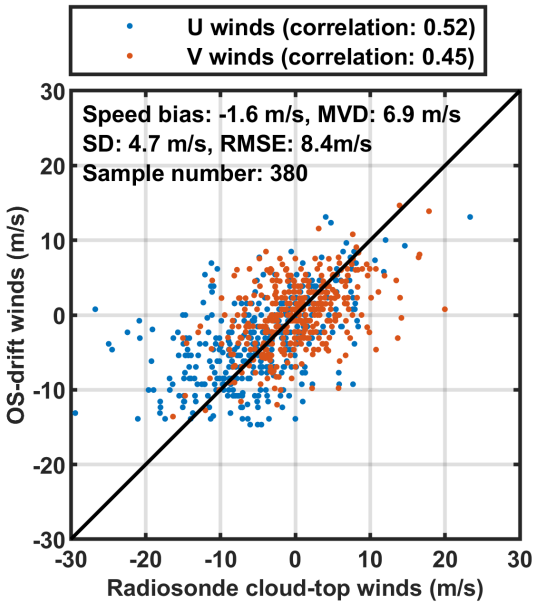

Figure 3. Comparisons of the U and V wind speeds between the tracked motions and radiosonde cloud-top winds within 150 km at Darwin, Manus and Nauru in 2006 with a total sample number of 380.

Quality control for missing images and the OSs touching the image edges is conducted. If the missing time gap between two continuous images exceeds 2 hours, the OSs in these two images and all lifecycles, including these OSs, are excluded from the analyses. Additionally, the OSs touching the image edges and all lifecycles, including the OSs touching edges, are excluded.

There are no direct observations to validate whether OSs are correctly associated. However, some of the tracked behaviors (e.g., the tracked motions of OSs) can be compared against the observations measured by other sensors. Only if the tracking is correct would the derived OS-drift winds perform well. Thus, the OS-drift winds are compared against the radiosonde cloud-top winds at three ARM tropical sites in Darwin, Manus and Nauru. Here, the cloud-top winds are derived by combining the radar and radiosonde observations at those sites (see more details in Sect. 2.3) as the observational reference to examine the tracked OS motions from the hourly satellite images in 2006. To collocate the observations from the ground-based sites and satellites, the tracked OS-drift winds from the GEO observations that are closest to the time of the cloud-top wind observations and nearest to the site locations are compared with the cloud-top winds at those ground-based sites. The observational time difference is no more than one hour and the tracked OS core centroid is within 150 km of those ARM site locations. These findings are consistent with those of previous studies in which the performance of cloud-drift winds is examined (Nieman et al., 1997; Santek et al., 2019; Daniels et al., 2020).

In Fig. 3, the OS-drift winds are significantly correlated with the radiosonde cloud-top winds. The correlations are 0.52 and 0.45 at the 99% significance level for the U and V wind components, respectively. On average, the OS-drift winds are slower than the radiosonde-observed winds, with a mean bias of -1.6 m/s. A slow speed bias of 1-2 m/s is common for cloud-drift winds (Santek et al., 2019). Owing to the limitations of the spatial and temporal resolutions (5 km and 1 hour, respectively), the least identifiable speed variation is approximately 5 km/hour (1.4 m/s), which is a possible reason for the slow speed bias. The bias in the mean angle is very small (0.5 degrees). The MVD, SD and RMSE are 6.9, 4.7 and 8.3 m/s, respectively. These biases are not surprising since real-world clouds do not strictly flow with ambient winds. In addition, some bias might be attributed to the uncertainty in the cloud-top heights. For its detection, the MMCR might underestimate the cloud top height since its signal would attenuate quickly for deep convective clouds (Hollars et al., 2004). In the convective systems, the motion of air is highly organized (Houze, 2004); thus, system movement might be inconsistent with the observed winds at the cloud-top height. Typically, the RMSE of the vector between the cloud-drift winds and the reference cloud-top winds is approximately 6-13 m/s, according to previous studies (Santek et al., 2019; Bresky et al., 2012). This finding indicates that the tracked motions

of OSs are reasonable and thereby variable-BT_{11} segment tracking is appropriate.

(5) Comparison with conventional fixed-threshold tracking

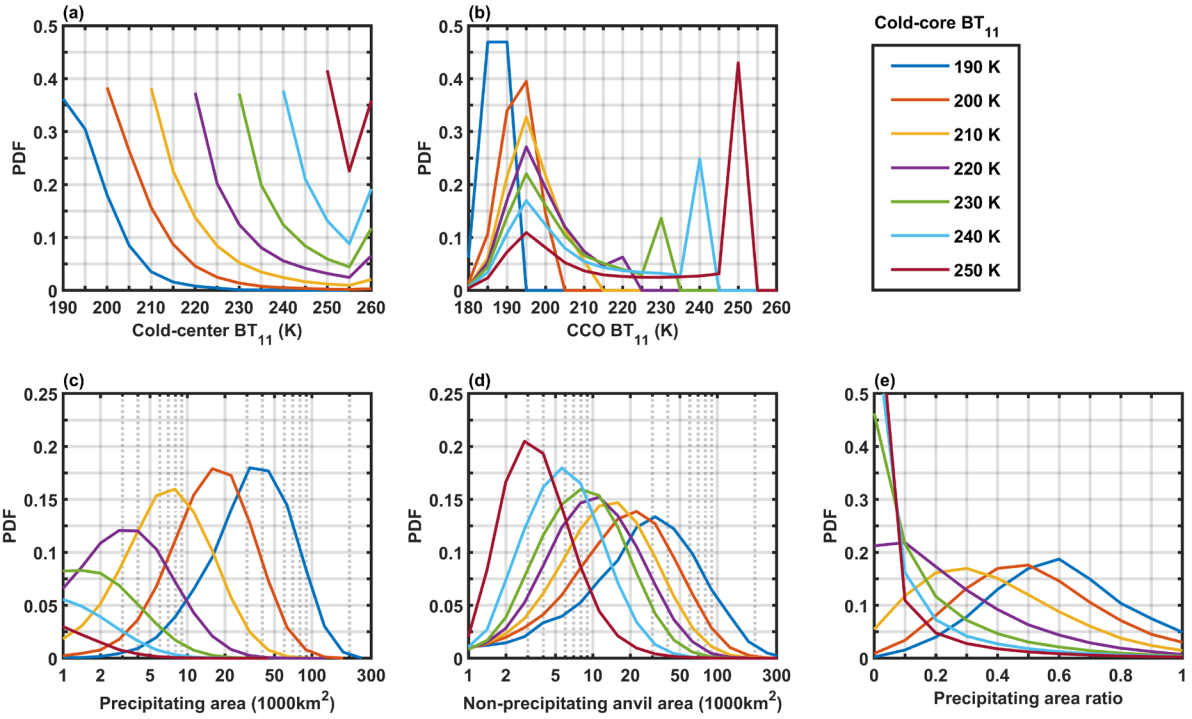

Figure 4. The OS characteristics of CCOs. PDFs of cold-center BT_{11} (a), CCO BT_{11} (b), the precipitating area (c), the non-precipitating area (d) and the ratio of the precipitating area (e) for the OSs of the cold-core BT_{11} from 190-250 K.

The fundamental difference between fixed-threshold and variable-BT_{11} tracking is target selection. With the fixed threshold of the BT_{11}, the connected convection of multiple cold cores is recognized as tracking targets, and only the area information is accessible. With the OS as tracking targets, variable-BT_{11} tracking is capable of documenting the detailed evolution of each OS within CCOs, such as the developing depth, connecting conditions, and contributions to precipitation and anvil clouds.

The complexity of convective organizations determines the use of fixed-threshold or variable-BT_{11} tracking. Specifically, if the structure of the convection is simple with only one cold core, it can be simply tracked via fixed-threshold tracking. Otherwise, for the complex organization of connected convective activities with multiple cold cores, variable-BT_{11} tracking is suitable since it is capable of segmenting CCOs into OSs for tracking. The complexity of convective organizations can be inferred from the cold-center BT_{11} of OSs. Only when the cold-center BT_{11} is 260 K is the OS of the isolated convective body. Under the fixed BT_{11} threshold, the OS of the cold-core BT_{11} that is warmer than the selected threshold cannot be identified. The OS of the cold-center BT_{11} that is colder than the selected threshold cannot be isolated from CCOs.

In Fig. 4, the OS characteristics (i.e., the connecting conditions with other surrounding OSs in CCOs and their contributions to precipitation and anvil cloud areas) of different developing depths with the cold-core BT_{11} from 190-250 K are investigated. In Fig. 4a, for the OSs of the cold core from 190-250 K, the probability distribution functions (PDFs) of the cold-center BT_{11} are shown. The PDF has a maximum peak of approximately 36-41% when the cold-center BT_{11} is equal to the cold-core BT_{11}. For example, if in the fixed-BT_{11} identification of the selected threshold of 220 K, only the OSs of the cold cores colder than 220 K and the cold centers warmer than 220 K can be isolated, but they account for only a small portion of the OSs of the cold-core BT_{11} of 190-210 K. This implies that even under the cold BT_{11} threshold, most of the identified targets still have complex organizations in the fixed-BT_{11} identification. The warmer the selected BT_{11} threshold is, the more complex the identified target is according to the fixed-threshold identification. The isolated structure with a cold-center BT_{11} of 260 K is rare for the deep convection of the cold-core BT_{11} at 190-220 K, but it is relatively more frequent and seems to be another

mode for the shallow warm systems of the cold-core BT_{11} at 230-260 K. However, fixed-threshold tracking is not capable of distinguishing which target is the complex or isolated structure.

Fig. 4b shows the PDFs of CCO BT_{11}, which refers to the coldest cold-core BT_{11} in the CCO. The CCO BT_{11} can help to further distinguish the connecting conditions of the OS at different depths of development. If the CCO BT_{11} is colder than the OS cold-core BT_{11}, the OS is in the deeper CCO and connected with the colder OS. Otherwise, if the CCO BT_{11} is equal to the OS cold-core BT_{11}, the OS is the isolated structure or connected with the warmer OS. For the OSs of the cold-core BT_{11} from 200-260 K, the PDFs of the CCO BT_{11} all peak at 195 K. It implies that they are the most frequently clustered in the 195-K CCO. For the OSs of cold-core BT_{11} from 230-260 K, another peak of the PDFs of their CCO BT_{11} is at their cold-core BT_{11}. Fig. 4a also shows that these OSs of the cold-core BT_{11} from 230-260 K are more likely to have their cold-center BT_{11} occur at 260 K. This implies that warm-core structures are more likely to be isolated as than cold-core structures. As a result, deep convective activities are mostly accompanied by the clustered complex organization, and variable-BT_{11} segment tracking is more suitable than fixed-threshold tracking for documenting their behaviors.

In variable-BT_{11} tracking, precipitation and anvil clouds can be explicitly associated with unique cold cores. In Figs. 4c-d, the distributions of the precipitation and anvil areas are lognormal and closely related to those of cold-core BT_{11}. The colder the cold-core BT_{11} is, the larger the precipitation and anvil areas to which the OS contributes. In Fig. 4e, the ratio of the OS precipitation area to the whole OS area is inversely proportional to the cold-core BT_{11}. Thus, the OSs of colder cores are dominated by precipitation, but these OSs still contribute to more anvil clouds than the OSs of warmer cores. Similar to Lindzen et al. (2001), the ratio of the OS precipitation area to the whole OS area can also be understood as diagnostic of the precipitation efficiency or detrainment effect. The results in Figs. 4c-e might imply that the OSs of colder cores have increased precipitation efficiency, which contributes to both more precipitation and anvil clouds.

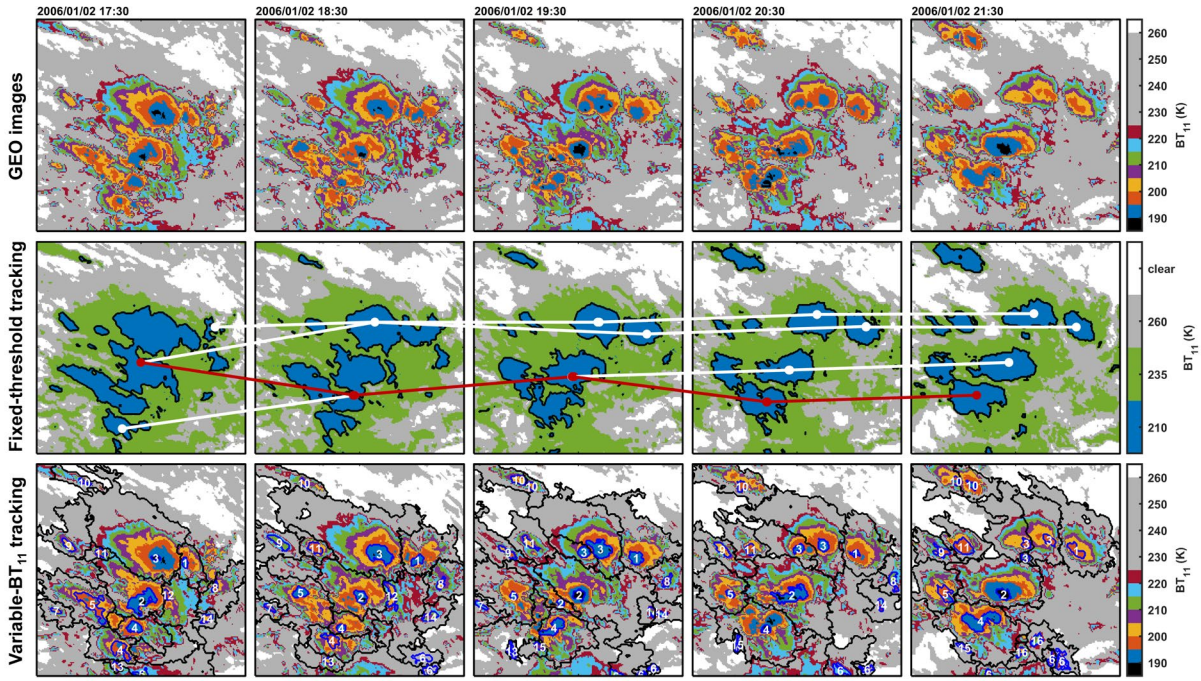

Figure 5. Examples illustrating the difference between conventional fixed-threshold tracking and novel variable-BT_{11} segment tracking. Uppermost panel: GEO BT_{11} images taken between 5°S-15°S and 120°E-130°E from January 2, 17:30 to 21:30 UTC in 2006. Middle panel: the tracked lifecycles based on the fixed thresholds of 210, 235 and 260 K. The white lines represent the tree of the tracked lifecycle under the fixed threshold of 210 K and the red lines represent the major branch obtained by selecting the largest area. Bottom panels: variable-BT_{11} identification and segment tracking. In the bottom panels, the blue contours indicate the cold cores, the black contours are the OSs in the CCOs, and the number at the core centroids indicates the lifecycle identification.

Examples of the conventional fixed-threshold and novel variable-BT_{11} tracking algorithms are shown in Fig. 5 to illustrate their differences. From the GEO images in the uppermost panel of Fig. 5, visually, those convective activities are connected

in CCOs but have distinct behaviors to decay, split, develop and merge over time. In the middle panel of Fig. 5, these behaviors of connected convections are barely distinguished by fixed-threshold tracking. With thresholds of 235 K and 260 K, the whole complex organization of connected convections is identified as the tracking target. By the cold threshold of 210 K, only a small part of the CCO is identified; nevertheless, those connected convections of distinct behaviors are still poorly distinguished. Additionally, in fixed-threshold tracking at 210 K, mergers and splits are caused by variations in whether convections are connected under the 210-K threshold. In this case, the tracked lifecycle tree is too complicated to analyze and is usually simplified by focusing only on the largest area at different times as the major lifecycle branch. The major branch (the red line in the middle panel of Fig. 5) begins with the large complex organization of connected convections but ends with only one of disconnected parts. Only the area information is available to describe the lifecycle in fixed-threshold tracking. In comparison, in the bottom panel of Fig. 5, on the basis of adaptive variable-BT_{11} identification and segment tracking, these connected convective activities are separately tracked as the decaying and splitting No. 3 OS, developing No. 2 OS, merging and developing No. 4 OS, etc. The mergers and splits of OSs are well tracked and not influenced by the variations in the connecting conditions over time. The area and cold-core BT_{11} information are both available to describe the tracked lifecycles.

4. Contributions of the OS lifecycles to the precipitation and anvil cloud amount

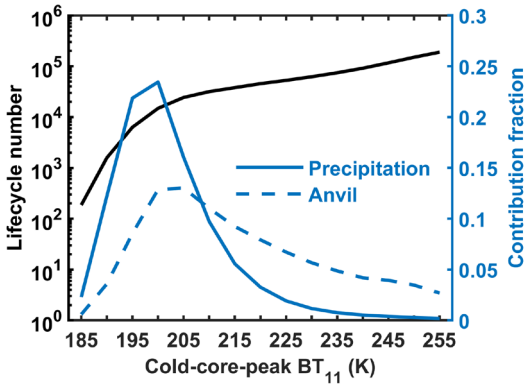

Figure 6. Sample numbers of tracked OS lifecycles with cold-core-peak BT_{11} values from 185-255 K in the tropical western Pacific (130°W-170°E, 20°S-20°N) in 2006. The contribution fraction of the OS lifecycles to the precipitation and anvil cloud amount is shown on the right axis.

The warm pool of the tropical western Pacific Ocean (130°W-170°E, 20°S-20°N) is a typical region of oceanic convection precipitating and producing anvil clouds (Wall et al., 2018). In this section, only the OS lifecycles over the oceans in this region are considered for investigating the behaviors of the oceanic convection precipitating and producing anvil clouds. On the basis of the tracked lifecycles, the total precipitation and anvil cloud amounts can be attributed to two factors: (1) the lifecycle occurrence frequency and (2) the convection precipitating and producing anvil clouds during each lifecycle. With the novel tracking dataset, these two aspects are investigated in this section.

For OS lifecycles, the cold-core-peak BT_{11} is identified as the coldest cold-core BT_{11} in lifecycles and is used to represent the convective peaking strength. The OS lifecycles can be classified by the cold-core-peak BT_{11}. In Fig. 6, the sample numbers of lifecycles of different cold-core-peak BT_{11} values over the tropical western Pacific Ocean in 2006 are shown. The warmer the cold-core-peak BT_{11} is, the greater the number of lifecycles is. The lifecycle of the cold-core-peak BT_{11} at 185 K has over one hundred samples, and the lifecycle of the cold-core-peak BT_{11} at 255 K has hundreds of thousands of samples in one year. In addition, Fig. 6 also shows the fractions of the contributions of OS lifecycles of different cold-core-peak BT_{11} values to the total precipitation and anvil cloud amounts. Here, the fraction of contribution refers to the sum of the precipitation (anvil) produced by all OS lifecycles in each bin of the cold-core-peak BT_{11} divided by the total precipitation (anvil). The OS lifecycles of the cold-core-peak BT_{11} at 200 K have the largest contribution to both the precipitation and anvil cloud amounts. Although the lifecycles of the cold-core-peak BT_{11} values warmer than 235 K include a great number of samples, those lifecycles contribute to only no more than 5% of the total precipitation and anvil cloud amounts. Nevertheless, those warm OS lifecycles

seem to be more important for anvil clouds than for precipitation.

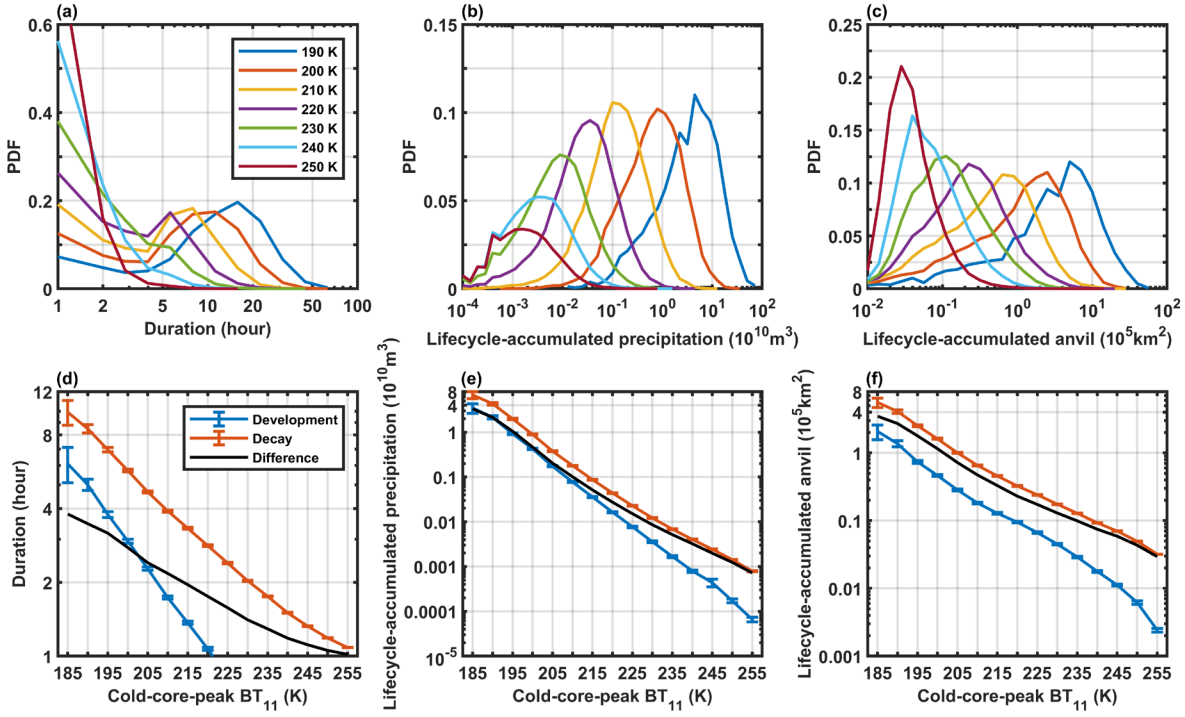

Figure 7. PDFs of the accumulated duration (a), precipitation (b) and non-precipitating anvil amount (c) of the OS lifecycles of different cold-core-peak BT_{11} values from 190-250 K. The mean accumulated duration (d), precipitation (e) and non-precipitating anvil amount (f) contributed by the development (blue lines) and decay stages (red lines) as a function of the cold-core-peak BT_{11} from 185-255 K. The black lines represent the differences in the accumulated duration, precipitation and anvil between the development and decay stages in (d-f), respectively. The error bars indicate the 95% confidence intervals of the means based on the t test.

In Figs. 7a-c, for different cold-core-peak BT_{11} values, the PDFs of the OS lifecycle-accumulated duration, precipitation and anvil amount are shown. In Fig. 7a, the PDFs of the duration of the cold-core-peak BT_{11} that is warmer than 220 K peaks at 1 hour and most of them are less than 5 hours, whereas the lifecycle of the cold-core-peak BT_{11} colder than 220 K has two modes for the short duration with the PDF peak at 1 hour and the long duration with the PDF peak at more than 5 hours. In Figs. 7b-c, the PDFs of the accumulated precipitation and anvil amounts contributed by the OS lifecycles basically conform to the lognormal distribution. Overall, the duration, precipitation and anvil amount of lifecycle accumulation are inversely proportional to the cold-core-peak BT_{11}.

In Figs. 7d-f, the relationships of the OS lifecycle-accumulated duration, precipitation and anvil amount with the cold-core-peak BT_{11} are further investigated. The OS lifecycle is separated into development and decay stages. The development (decay) stage is defined as the stage before (after) the cold core peaks at the coldest BT_{11} with the largest core area. In Fig. 7d, only the OS lifecycles of the cold-core-peak BT_{11} colder than 220 K have a development of more than 1 hour, whereas the OS lifecycles of the peak BT_{11} that is warmer than 220 K directly decay and disappear rapidly within a few hours. Figs. 7d-f show that the process of decay is longer than the process of development and that more precipitation and anvil clouds are contributed by the process of decay that by the process of development. Overall, the OS lifecycle-accumulated duration, precipitation and anvil amount have simple loglinear relationships with the peak BT_{11} in both the development and decay stages. The difference in the accumulated duration, precipitation and anvil cloud amounts between the two stages (the black line in Figs. 7d-f) also exponentially increases, with the core peaking at colder BT_{11} values. The duration of the development and decay processes and the two key components of the convective cloud water budget, i.e., the lifecycle-accumulated precipitation and anvil cloud amounts, are closely related to the peaking cold-core structures.

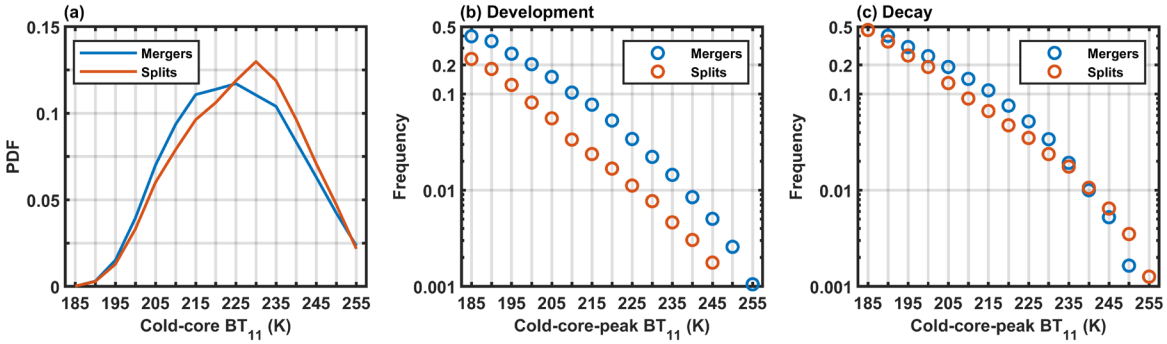

Figure 8. (a) PDFs of BT_{11} values for mergers (blue lines) and splits (red lines). The frequency of merger and split occurrence in the lifecycles of the cold-core-peak BT_{11} from 185-255 K in the development (b) and decay (c) stages.

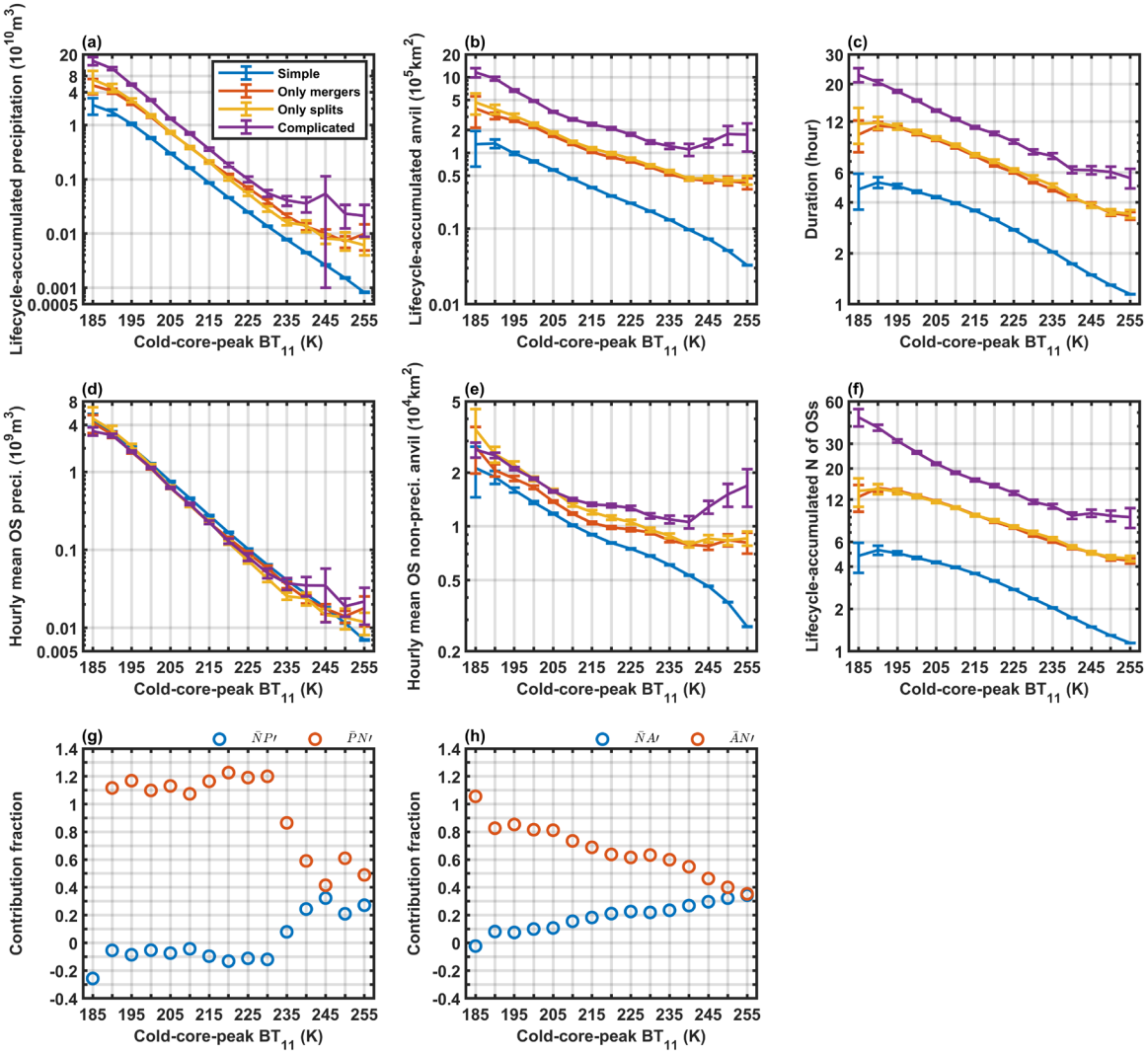

Figure 9. (a-c) Composites of the lifecycle-accumulated precipitation, anvil cloud amounts and duration of different lifecycle types in each bin of the cold-core-peak BT_{11} from 185-255 K, respectively. (d-e) Composites of the hourly mean OS precipitation and anvil cloud amounts, and the lifecycle-accumulated number of OSs of different lifecycle types in each bin of the cold-core-peak BT_{11}, respectively. The blue, red, yellow and purple lines indicate the simple, only-merger, only-split and complicated lifecycles, respectively. (g) The fractions of contributions of the OS hourly precipitation and the lifecycle-accumulated OS number of anomalies to the variation in lifecycle-accumulated precipitation. (h) The fractions of contributions of the OS hourly anvil production and the lifecycle-accumulated OS number of anomalies to the variation in the lifecycle-accumulated anvil amount. The error bars indicate the 95% confidence intervals of the means based on the t test.

In Fig. 8a, according to the PDFs of the cold-core BT_{11} of mergers and splits, the cold-core BT_{11} of mergers is more distributed at colder BT_{11} values than that of splits. This implies that mergers are more likely to occur for the OSs of cold BT_{11}

values, whereas splits are more likely to occur for the OSs of warm BT_{11} values. In Figs. 8b-c, according to the frequency of merger and split occurrence in the OS lifecycles of different cold-core-peak BT_{11} values, in both the development and decay stages, it is somewhat surprising that the frequency of mergers and splits still has a loglinear relationship with the cold-core-peak BT_{11}. In the development process, mergers are more likely to occur than splits. In the decay process, mergers and splits have similar frequencies, but the splits in the decay process are more frequent than those in the development process.

According to the occurrence of mergers and splits, OS lifecycles can be further classified into simple (no mergers or splits), only-merger, only-split and complicated (both mergers and splits) types. In Figs. 9a-c, the lifecycle-accumulated precipitation, anvil cloud amounts and duration are strongly related to the occurrence of mergers and splits. For the same cold-core-peak BT_{11}, the complicated lifecycles have the largest accumulated precipitation, anvil and duration among all lifecycle types. The only-merger and only-split lifecycles have similar accumulated precipitation, anvil and duration values that are greater than those of the simple lifecycles. Interestingly, for different types of lifecycles, the slopes of the loglinear relationships of the lifecycle-accumulated precipitation, anvil and duration, with the cold-core-peak BT_{11}, are nearly invariant. This implies that mergers and splits do not influence the dependence of the lifecycle-accumulated precipitation and anvil cloud amounts on the BT_{11} structures and that the increased precipitation and anvil cloud amounts caused by the mergers and splits also conform to a loglinear relationship with the cold-core-peak BT_{11}.

How do mergers and splits influence the lifecycle-accumulated precipitation and anvil cloud amounts? There are two possible mechanisms: the hourly precipitation and anvil production of each OS in the lifecycle are enhanced, and the accumulated number (N) of OSs in the lifecycle is increased. In Figs. 9d-f, the hourly mean precipitation and anvil amount of each OS and N of OSs are shown for different lifecycle types. For the same cold-core-peak BT_{11}, the hourly mean OS precipitation of different lifecycle types (Fig. 9d) is nearly invariant. The hourly mean anvil production of OSs (Fig. 9e) is greater in the lifecycles with the occurrence of mergers and splits than in the simple lifecycles. In Fig. 9f, the accumulated N of OSs has the most significant variation for different lifecycle types. For the same cold-core-peak BT_{11}, N in the complicated lifecycles is much larger than the N of the other lifecycles. For the only-merger and only-split lifecycles, N is nearly the same and much greater than the N of the simple lifecycles. Thus, for different lifecycle types of mergers and splits, the variation in lifecycle-accumulated precipitation is influenced mostly by the N of OSs, whereas the lifecycle-accumulated anvil amount is influenced by both the hourly anvil production in each OS and the N of OSs.

Accordingly, in Figs. 9g-h, the anomalies of the lifecycle-accumulated precipitation and anvil cloud amounts can be decomposed as follows:

$$PN - \bar{P}\bar{N} = \bar{N}P' + \bar{P}N' + P'N', \tag{7}$$

$$AN - \bar{A}\bar{N} = \bar{N}A' + \bar{A}N' + A'N'. \tag{8}$$

P and A are the OS hourly precipitation and anvil cloud amount, respectively. N is the accumulated OS number in the lifecycle. Thus, PN and AN represent the lifecycle-accumulated precipitation and anvil cloud amount, respectively. The bar over the letter represents the mean of different lifecycle types, and the prime represents the anomaly due to the different lifecycle types. In this way, $\bar{N}P'$ and $\bar{P}N'$ indicate the contributions of the OS hourly precipitation anomaly and the OS number anomaly, respectively, to the variation in lifecycle-accumulated precipitation. Similarly, $\bar{N}A'$ and $\bar{A}N'$ indicate the contributions of the OS hourly anvil production and number anomalies, respectively, to the variation in the lifecycle-accumulated anvil amount. $P'N'$ and $A'N'$ are high-order small quantities and are neglected. The fraction of the contribution can be computed by dividing the left-hand-side quantities of Eq. 7 and Eq. 8. Figs. 9g-h show the fractions of the contributions of $\bar{N}P'$ and $\bar{P}N'$ ($\bar{N}A'$ and $\bar{A}N'$) to the increase in the lifecycle-accumulated precipitation (anvil) from the simple to complicated lifecycles. For the long-lived lifecycles of cold-core-peak BT_{11} values colder than 220 K, $\bar{N}P'$ has a small negative contribution of approximately -10%, whereas $\bar{P}N'$ has a large contribution of approximately 110%. And $\bar{N}A'$ and $\bar{A}N'$ both have positive fractions of contribution of approximately 0-20% and 65-105%, respectively. For the short-lived warmer lifecycles, although the

contributions from $\overline{N}P'$ and $\overline{N}A'$ increase, the N anomaly still makes the greatest contribution to the variation in the lifecycle-accumulated precipitation and anvil cloud amounts. Overall, in comparison with simple lifecycles, the mergers and splits can create more OSs whose precipitation is slightly reduced and anvil production is enhanced, to ultimately prolong lifetime and increase both precipitation and anvil clouds of the lifecycle accumulation.

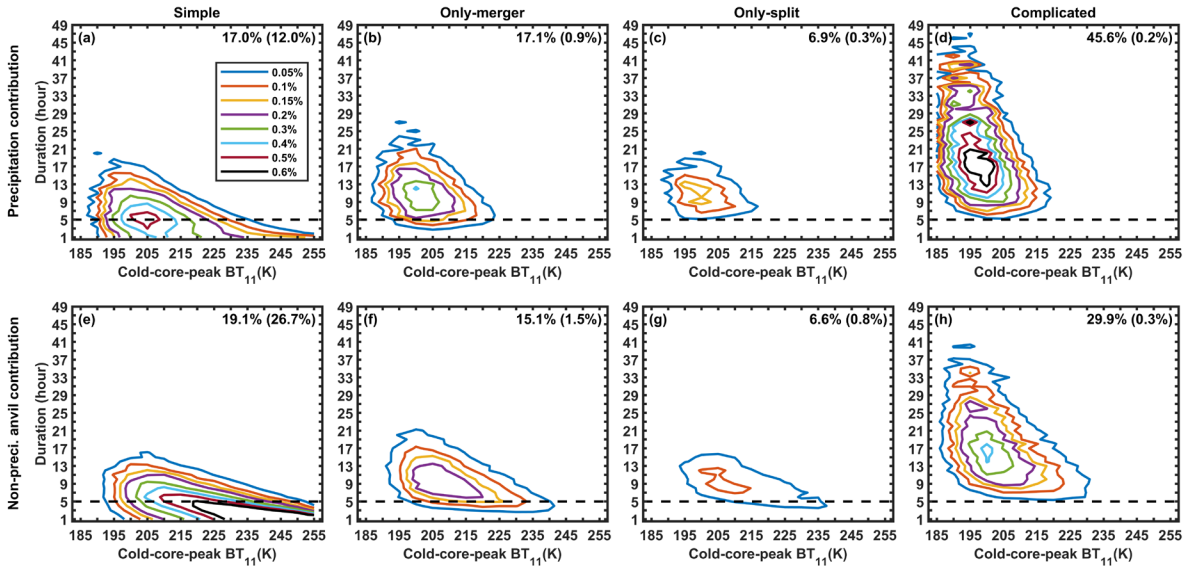

Figure 10. Fractions of the contribution of the OS lifecycles of different cold-core-peak BT_{11} values and durations to the total precipitation (a-d) and anvil cloud amount (e-h) over the tropical western Pacific Ocean for simple, only-merger, only-split and complicated lifecycles, respectively. In each panel, the fractions of contributions of the long-lived (short-lived) lifecycles of durations larger (less) than 5 hours are listed in the top right-hand corner.

In Figs. 7-9, the OS lifecycle-accumulated duration, precipitation and anvil cloud amounts have a loglinear relationship with the cold-core-peak BT_{11} and are positively related to the occurrence of mergers and splits. However, cold lifecycles are less common than warm lifecycles and thus might make only small contributions to the total precipitation and anvil clouds (Fig. 6). In Fig. 10, the contributions of the OS lifecycles of different cold-core-peak BT_{11} values and durations to the total precipitation and anvil cloud amounts are shown. For precipitation, as shown in Figs. 10a-d, the complicated lifecycles have the largest contribution of 45.8%, compared with the simple (29%), only-merger (18%) and only-split (7.2%) lifecycles. The long-lived lifecycles of the duration at least 5 hours contribute to 86.6% of the total precipitation. For the non-precipitating anvil clouds in Figs. 10e-h, the long-lived complicated lifecycles and short-lived (less than 5 hours) simple lifecycles are both important, with contribution fractions of 29.9% and 26.7%, respectively. The complicated long-lived lifecycles, whose cold-core-peak BT_{11} is mostly less than 220 K, are efficient at producing anvil clouds but are less frequent. The short-lived simple lifecycles, whose cold-core-peak BT_{11} are mostly greater than 220 K are not efficient at producing anvil clouds but are very frequent.

5. Conclusion

Tropical convection organizations are normally connected complexes of many convective activities. In this work, a novel variable-BT_{11} segment tracking algorithm is established to segment the CCO into OSs for tracking. The tracked motions of OSs are compared against the observational winds to examine the rationality of tracking. Strong correlations between the tracked motions and real winds are found, with small differences in the mean speeds (-1.6 m/s) and angles (0.5°). These results confirm that tracking is appropriate.

Compared with the previous fixed-threshold and variable-BT_{11} tracking algorithms that focus only on the variation in the area, the novel tracking algorithm developed in this work is capable of documenting the evolution of both the area and BT_{11} structure (i.e., the cold-core and cold-center BT_{11} for indicating the developing and connecting conditions, respectively, and mergers and splits of cold cores). Precipitation and anvil clouds are explicitly associated with unique cold cores. The lifecycles

are described by the variation in the cold-core BT_{11}, e.g., cold-core-peak BT_{11}, merger and split BT_{11}. The major difference between the fixed-threshold and novel variable-BT_{11} tracking algorithms is the selection of tracking targets. The complex organizations of multiple cold cores are very frequent, and isolated convective bodies are rare, particularly for the deep convection of the cold-core BT_{11} from 190-220 K. This implies that most of the targets identified by the fixed BT_{11} threshold are complex organizations and their segmentation by the variable-BT_{11} tracking algorithm is necessary. Additionally, in fixed-threshold tracking, mergers and splits are caused by many reasons: threshold selection, changes in the connecting conditions, and variations in the clod cores. This makes the final lifecycle in fixed-threshold tracking very complicated. In contrast, mergers and splits of cold cores in the variable-BT_{11} tracking algorithm can be well captured and not influenced by the variation in the connecting conditions.

On the basis of the novel variable-BT_{11} tracking algorithm, the convective processes of precipitation and the production of anvil clouds over the tropical western Pacific Ocean are investigated. Interestingly, the accumulated duration, precipitation and anvil cloud amounts produced from the OS lifecycles have simple loglinear relationships with the BT_{11} of the cold core peak. Most of the lifecycles of the cold-core-peak BT_{11} values colder than 220 K are long-lived, with durations of more than 5 hours. The lifecycles of the warmer-peak BT_{11} are short-lived. During the lifecycle, decay requires more time than development does. More accumulated precipitation and anvil cloud amounts are also contributed by the decay stage than by the development stage. The difference in the accumulated duration, precipitation and anvil production between the two stages increases exponentially with decreasing cold-core-peak BT_{11}.

The occurrence of mergers and splits also strongly relies on the BT_{11} of the cold core peak, which still has a loglinear relationship. Overall, mergers are more frequent than splits are in the development stage. In the decay stage, the frequency of mergers and splits shows little difference. The frequency of splits in the decay stage is greater than that in the development stage. Lifecycle-accumulated precipitation and anvil production are positively related to the occurrence of mergers and splits. With the same cold-core-peak BT_{11}, the increase in the lifecycle-accumulated precipitation between the simple and complicated lifecycles is mostly attributed to the increase in the number of OSs during the lifecycle. The increase in the lifecycle-accumulated anvil cloud amount between the simple and complicated lifecycles should be attributed to the increase in both the hourly anvil production in each OS and the number of OSs. The slope of the loglinear relationship between the lifecycle-accumulated precipitation or anvil and the cold-core-peak BT_{11} is almost invariant for different lifecycle types.

Although the lifecycles of cold peaking cores are more efficient at precipitating and producing anvil clouds, it occurrence frequency is much lower than that of warm peaking cores. For the total cloud water budget of the tropical western Pacific Ocean, most of the total precipitation (45.6%) is contributed by long-lived complicated lifecycles, whereas short-lived simple lifecycles are less important for precipitation, with a contribution of 12%. However, for the anvil cloud amount, the long-lived complicated lifecycle and the short-lived simple lifecycle are both important, with contributions of 29.9% and 26.7%, respectively.

Acknowledgment

This work was supported by the NSFC-41875004 and the National Key R&D Program of China (2016YFC0202000).

Author contribution

ZW and JY designed the algorithm. ZW carried out the experiment and prepared the manuscript.

Data and code availability

All data used in this study are available online. The GEO images (Nasa/Larc/Sd/Asdc, 2017) are obtained from the National Aeronautics and Space Administration (NASA) Langley Research Center Atmospheric Science Data Center (https://search.earthdata.nasa.gov/). GPM (Huffman, 2023) is obtained from the Goddard Earth Sciences Data and Information Services Center (GES DISC). The ground-based cloud (S. Giangrande, 1999) and wind (E. Keeler, 2001) observations at the

ground-based sites are obtained from the Atmospheric Radiation Measurement user facility, a U.S. Department Of Energy (DOE) office of science user facility managed by the biological and environmental research program (https://www.arm.gov). The code of the anvil tracking algorithm is available upon request.

Competing interests

The author declares no conflict of interest.

Reference

Amidror, I.: Scattered data interpolation methods for electronic imaging systems: a survey, Journal of Electronic Imaging, 11, 10.1117/1.1455013, 2002.

Atlas, R. L., Bretherton, C. S., Sokol, A. B., Blossey, P. N., and Khairoutdinov, M. F.: Tropical Cirrus Are Highly Sensitive to Ice Microphysics Within a Nudged Global Storm-Resolving Model, Geophysical Research Letters, 51, 10.1029/2023gl105868, 2024.

Bao, J. and Sherwood, S. C.: The Role of Convective Self-Aggregation in Extreme Instantaneous Versus Daily Precipitation, Journal of Advances in Modeling Earth Systems, 11, 19-33, 10.1029/2018ms001503, 2019.

Blossey, P. N., Bretherton, C. S., and Khairoutdinov, M.: An Energy-Balance Analysis of Deep Convective Self-Aggregation above Uniform SST, Journal of the Atmospheric Sciences, 62, 4273-4292, 10.1175/jas3614.1, 2005.

Blossey, P. N., Bretherton, C. S., Cetrone, J., and Kharoutdinov, M.: Cloud-Resolving Model Simulations of KWAJEX: Model Sensitivities and Comparisons with Satellite and Radar Observations, Journal of the Atmospheric Sciences, 64, 1488-1508, 10.1175/jas3982.1, 2007.

Bony, S., Semie, A., Kramer, R. J., Soden, B., Tompkins, A. M., and Emanuel, K. A.: Observed Modulation of the Tropical Radiation Budget by Deep Convective Organization and Lower-Tropospheric Stability, AGU Advances, 1, 10.1029/2019av000155, 2020.

Bouniol, D., Roca, R., Fiolleau, T., and Poan, D. E.: Macrophysical, Microphysical, and Radiative Properties of Tropical Mesoscale Convective Systems over Their Life Cycle, Journal of Climate, 29, 3353-3371, 10.1175/jcli-d-15-0551.1, 2016.

Bresky, W. C., Daniels, J. M., Bailey, A. A., and Wanzong, S. T.: New Methods toward Minimizing the Slow Speed Bias Associated with Atmospheric Motion Vectors, Journal of Applied Meteorology and Climatology, 51, 2137-2151, 10.1175/jamc-d-11-0234.1, 2012.

Bretherton, C. S.: Insights into low-latitude cloud feedbacks from high-resolution models, Philos Trans A Math Phys Eng Sci, 373, 10.1098/rsta.2014.0415, 2015.

Bretherton, C. S., Widmann, M., Dymnikov, V. P., Wallace, J. M., and Bladé, I.: The Effective Number of Spatial Degrees of Freedom of a Time-Varying Field, Journal of Climate, 12, 1990-2009, 10.1175/1520-0442(1999)012<1990:Tenosd>2.0.Co;2, 1999.

Chen, S. S. and Houze, R. A.: Diurnal variation and life-cycle of deep convective systems over the tropical pacific warm pool, Quarterly Journal of the Royal Meteorological Society, 123, 357-388, 10.1002/qj.49712353806, 1997.

Clement, A. C. and Soden, B.: The Sensitivity of the Tropical-Mean Radiation Budget, Journal of Climate, 18, 3189-3203, 10.1175/jcli3456.1, 2005.

Coppin, D. and Bony, S.: Physical mechanisms controlling the initiation of convective self-aggregation in a General Circulation Model, Journal of Advances in Modeling Earth Systems, 7, 2060-2078, 10.1002/2015ms000571, 2015.

Daniels, J., Bresky, W., Bailey, A., Allegrino, A., Velden, C. S., and Wanzong, S.: Chapter 8 - Winds from ABI on the GOES-R Series, in: The GOES-R Series, edited by: Goodman, S. J., Schmit, T. J., Daniels, J., and Redmon, R. J., Elsevier, 79-94, https://doi.org/10.1016/B978-0-12-814327-8.00008-1, 2020.

de Laat, A., Defer, E., Delanoë, J., Dezitter, F., Gounou, A., Grandin, A., Guignard, A., Meirink, J. F., Moisselin, J.-M., and Parol, F.: Analysis of geostationary satellite-derived cloud parameters associated with environments with high ice water content, Atmospheric Measurement Techniques, 10, 1359-1371, 10.5194/amt-10-1359-2017, 2017.

Doelling, D. R., Sun, M., Nguyen, L. T., Nordeen, M. L., Haney, C. O., Keyes, D. F., and Mlynczak, P. E.: Advances in Geostationary-Derived Longwave Fluxes for the CERES Synoptic (SYN1deg) Product, Journal of Atmospheric and Oceanic Technology, 33, 503-521, 10.1175/jtech-d-15-0147.1, 2016.

Doelling, D. R., Loeb, N. G., Keyes, D. F., Nordeen, M. L., Morstad, D., Nguyen, C., Wielicki, B. A., Young, D. F., and Sun, M.: Geostationary Enhanced Temporal Interpolation for CERES Flux Products, Journal of Atmospheric and Oceanic Technology, 30, 1072-1090, 10.1175/jtech-d-12-00136.1, 2013.

E. Keeler, K. B. a. J. K.: Balloon-Borne Sounding System (SONDEWNPN), ARM Data Center, 10.5439/1595321, 2001.

Feidas, H. and Cartalis, C.: Application of an automated cloud-tracking algorithm on satellite imagery for tracking and monitoring small mesoscale convective cloud systems, International Journal of Remote Sensing, 26, 1677-1698, 10.1080/01431160512331338023, 2007.

Feng, Z., Hardin, J., Barnes, H. C., Li, J., Leung, L. R., Varble, A., and Zhang, Z.: PyFLEXTRKR: a flexible feature tracking Python software for convective cloud analysis, Geoscientific Model Development, 16, 2753-2776, 10.5194/gmd-16-2753-2023, 2023.

Fiolleau, T. and Roca, R.: An Algorithm for the Detection and Tracking of Tropical Mesoscale Convective Systems Using Infrared Images From Geostationary Satellite, IEEE Transactions on Geoscience and Remote Sensing, 51, 4302-4315, 10.1109/tgrs.2012.2227762, 2013.

Fu, R., Del Genio, A. D., and Rossow, W. B.: Behavior of Deep Convective Clouds in the Tropical Pacific Deduced from ISCCP Radiances, Journal of Climate, 3, 1129-1152, 10.1175/1520-0442(1990)003<1129:Bodcci>2.0.Co;2, 1990.

Fu, Y., Sun, J., Fu, S., Zhang, Y., and Ma, Z.: Initiations of Mesoscale Convective Systems in the Middle Reaches of the Yangtze River Basin Based on FY-4A Satellite Data: Statistical Characteristics and Environmental Conditions, Journal of Geophysical Research: Atmospheres, 128, 10.1029/2023jd038630, 2023.

Goyens, C., Lauwaet, D., Schröder, M., Demuzere, M., and Van Lipzig, N. P. M.: Tracking mesoscale convective systems in the Sahel: relation between cloud parameters and precipitation, International Journal of Climatology, 32, 1921-1934, 10.1002/joc.2407, 2011.

Heikenfeld, M., Marinescu, P. J., Christensen, M., Watson-Parris, D., Senf, F., van den Heever, S. C., and Stier, P.: tobac 1.2: towards a flexible framework for tracking and analysis of clouds in diverse datasets, Geoscientific Model Development, 12, 4551-4570, 10.5194/gmd-12-4551-2019, 2019.

Hendon, H. H. and Woodberry, K.: The diurnal cycle of tropical convection, Journal of Geophysical Research, 98, 10.1029/93jd00525, 1993.

Hersbach, H., Bell, B., Berrisford, P., Hirahara, S., Horányi, A., Muñoz-Sabater, J., Nicolas, J., Peubey, C., Radu, R., Schepers, D., Simmons, A., Soci, C., Abdalla, S., Abellan, X., Balsamo, G., Bechtold, P., Biavati, G., Bidlot, J., Bonavita, M., Chiara, G., Dahlgren, P., Dee, D., Diamantakis, M., Dragani, R., Flemming, J., Forbes, R., Fuentes, M., Geer, A., Haimberger, L., Healy, S., Hogan, R. J., Hólm, E., Janisková, M., Keeley, S., Laloyaux, P., Lopez, P., Lupu, C., Radnoti, G., Rosnay, P., Rozum, I., Vamborg, F., Villaume, S., and Thépaut, J. N.: The ERA5 global reanalysis, Quarterly Journal of the Royal Meteorological Society, 146, 1999-2049, 10.1002/qj.3803, 2020.

Hollars, S., Fu, Q., Comstock, J., and Ackerman, T.: Comparison of cloud-top height retrievals from ground-based 35 GHz MMCR and GMS-5 satellite observations at ARM TWP Manus site, Atmospheric Research, 72, 169-186, 10.1016/j.atmosres.2004.03.015, 2004.

Holloway, C. E., Wing, A. A., Bony, S., Muller, C., Masunaga, H., L'Ecuyer, T. S., Turner, D. D., and Zuidema, P.: Observing Convective Aggregation, Surveys in Geophysics, 38, 1199-1236, 10.1007/s10712-017-9419-1, 2017.

Houze, R. A.: Mesoscale convective systems, Reviews of Geophysics, 42, 10.1029/2004rg000150, 2004.

Huang, X., Hu, C., Huang, X., Chu, Y., Tseng, Y.-h., Zhang, G. J., and Lin, Y.: A long-term tropical mesoscale convective systems dataset based on a novel objective automatic tracking algorithm, Climate Dynamics, 51, 3145-3159, 10.1007/s00382-018-4071-0, 2018.

Huffman, G. J., Adler, R. F., Bolvin, D. T., Gu, G., Nelkin, E. J., Bowman, K. P., Hong, Y., Stocker, E. F., and Wolff, D. B.: The TRMM Multisatellite Precipitation Analysis (TMPA): Quasi-Global, Multiyear, Combined-Sensor Precipitation Estimates at Fine Scales,

Journal of Hydrometeorology, 8, 38-55, 10.1175/jhm560.1, 2007.

Huffman, G. J., Adler, R. F., Arkin, P., Chang, A., Ferraro, R., Gruber, A., Janowiak, J., McNab, A., Rudolf, B., and Schneider, U.: The Global Precipitation Climatology Project (GPCP) Combined Precipitation Dataset, Bulletin of the American Meteorological Society, 78, 5-20, 10.1175/1520-0477(1997)078<0005:Tgpcpg>2.0.Co;2, 1997.

Huffman, G. J., E.F. Stocker, D.T. Bolvin, E.J. Nelkin, Jackson Tan: GPM IMERG Final Precipitation L3 Half Hourly 0.1 degree x 0.1 degree V07, Goddard Earth Sciences Data and Information Services Center (GES DISC), 10.5067/GPM/IMERG/3B-HH/07, 2023.

Kolios, S. and Feidas, H.: A warm season climatology of mesoscale convective systems in the Mediterranean basin using satellite data, Theoretical and Applied Climatology, 102, 29-42, 10.1007/s00704-009-0241-7, 2009.

Laing, A. G., Carbone, R., Levizzani, V., and Tuttle, J.: The propagation and diurnal cycles of deep convection in northern tropical Africa, Quarterly Journal of the Royal Meteorological Society, 134, 93-109, 10.1002/qj.194, 2008.

Leese, J. A., Novak, C. S., and Clark, B. B.: An Automated Technique for Obtaining Cloud Motion from Geosynchronous Satellite Data Using Cross Correlation, Journal of Applied Meteorology, 10, 118-132, 10.1175/1520-0450(1971)010<0118:Aatfoc>2.0.Co;2, 1971.

Lindzen, R. S., Chou, M.-D., and Hou, A. Y.: Does the Earth Have an Adaptive Infrared Iris?, Bulletin of the American Meteorological Society, 82, 417-432, 10.1175/1520-0477(2001)082<0417:Dtehaa>2.3.Co;2, 2001.

Matsui, T., Zeng, X., Tao, W.-K., Masunaga, H., Olson, W. S., and Lang, S.: Evaluation of Long-Term Cloud-Resolving Model Simulations Using Satellite Radiance Observations and Multifrequency Satellite Simulators, Journal of Atmospheric and Oceanic Technology, 26, 1261-1274, 10.1175/2008jtecha1168.1, 2009.

Mauritsen, T. and Stevens, B.: Missing iris effect as a possible cause of muted hydrological change and high climate sensitivity in models, Nature Geoscience, 8, 346-351, 10.1038/ngeo2414, 2015.

Merrill, R. T., Menzel, W. P., Baker, W., Lynch, J., and Legg, E.: A Report on the Recent Demonstration of NOAA's Upgraded Capability to Derive Cloud Motion Satellite Winds, Bulletin of the American Meteorological Society, 72, 372-376, 10.1175/1520-0477-72.3.372, 1991.

Muller, C. and Bony, S.: What favors convective aggregation and why?, Geophysical Research Letters, 42, 5626-5634, 10.1002/2015gl064260, 2015.

NASA/LARC/SD/ASDC: SatCORPS CERES GEO Edition 4 MTSAT-1R Version 1.0, NASA Langley Atmospheric Science Data Center DAAC, 2017.

Nieman, S. J., Menzel, W. P., Hayden, C. M., Gray, D., Wanzong, S. T., Velden, C. S., and Daniels, J.: Fully Automated Cloud-Drift Winds in NESDIS Operations, Bulletin of the American Meteorological Society, 78, 1121-1133, 10.1175/1520-0477(1997)078<1121:Facdwi>2.0.Co;2, 1997.

Powell, S. W., Houze, R. A., Kumar, A., and McFarlane, S. A.: Comparison of Simulated and Observed Continental Tropical Anvil Clouds and Their Radiative Heating Profiles, Journal of the Atmospheric Sciences, 69, 2662-2681, 10.1175/jas-d-11-0251.1, 2012.

Rennó, N. O., Emanuel, K. A., and Stone, P. H.: Radiative-convective model with an explicit hydrologic cycle: 1. Formulation and sensitivity to model parameters, Journal of Geophysical Research: Atmospheres, 99, 14429-14441, 10.1029/94jd00020, 1994.

Richards, F. and Arkin, P.: On the Relationship between Satellite-Observed Cloud Cover and Precipitation, Monthly Weather Review, 109, 1081-1093, 10.1175/1520-0493(1981)109<1081:Otrbso>2.0.Co;2, 1981.

Ruppert, J. H. and Hohenegger, C.: Diurnal Circulation Adjustment and Organized Deep Convection, Journal of Climate, 31, 4899-4916, 10.1175/jcli-d-17-0693.1, 2018.

S. Giangrande, E. C. a. P. K.: Active Remote Sensing of CLouds (ARSCL1CLOTH), ARM Data Center, 10.5439/1996113, 1999.

Salonen, K. and Bormann, N.: Atmospheric Motion Vector observations in the ECMWF system: Fifth year report, 2016.

Santek, D., Dworak, R., Nebuda, S., Wanzong, S., Borde, R., Genkova, I., García-Pereda, J., Galante Negri, R., Carranza, M., Nonaka, K., Shimoji, K., Oh, S. M., Lee, B.-I., Chung, S.-R., Daniels, J., and Bresky, W.: 2018 Atmospheric Motion Vector (AMV)

Intercomparison Study, Remote Sensing, 11, 10.3390/rs11192240, 2019.

Schröder, M., König, M., and Schmetz, J.: Deep convection observed by the Spinning Enhanced Visible and Infrared Imager on board Meteosat 8: Spatial distribution and temporal evolution over Africa in summer and winter 2006, Journal of Geophysical Research: Atmospheres, 114, 10.1029/2008jd010653, 2009.

Sokol, A. B. and Hartmann, D. L.: Congestus Mode Invigoration by Convective Aggregation in Simulations of Radiative-Convective Equilibrium, J Adv Model Earth Syst, 14, e2022MS003045, 10.1029/2022MS003045, 2022.

Suzuki, K., Golaz, J. C., and Stephens, G. L.: Evaluating cloud tuning in a climate model with satellite observations, Geophysical Research Letters, 40, 4464-4468, 10.1002/grl.50874, 2013.

Tian, Y., Peters-Lidard, C. D., Eylander, J. B., Joyce, R. J., Huffman, G. J., Adler, R. F., Hsu, K. l., Turk, F. J., Garcia, M., and Zeng, J.: Component analysis of errors in satellite-based precipitation estimates, Journal of Geophysical Research: Atmospheres, 114, 10.1029/2009jd011949, 2009.

Tobin, I., Roca, R., and Bony, S.: Observational Evidence for Relationships between the Degree of Aggregation of Deep Convection, Water Vapor, Surface Fluxes, and Radiation, Journal of Climate, 25, 6885-6904, 10.1175/jcli-d-11-00258.1, 2012.

Tsakraklides, G. and Evans, J. L.: Global and regional diurnal variations of organized convection, Journal of Climate, 16, 1562-1572, Doi 10.1175/1520-0442-16.10.1562, 2003.

Velden, C. S., Olander, T. L., and Wanzong, S.: The Impact of MultispectralGOES-8Wind Information on Atlantic Tropical Cyclone Track Forecasts in 1995. Part I: Dataset Methodology, Description, and Case Analysis, Monthly Weather Review, 126, 1202-1218, 10.1175/1520-0493(1998)126<1202:Tiomgw>2.0.Co;2, 1998.

Wall, C. J., Hartmann, D. L., Thieman, M. M., Smith, W. L., and Minnis, P.: The Life Cycle of Anvil Clouds and the Top-of-Atmosphere Radiation Balance over the Tropical West Pacific, Journal of Climate, 31, 10059-10080, 10.1175/jcli-d-18-0154.1, 2018.

Williams, M. and Houze, R. A.: Satellite-Observed Characteristics of Winter Monsoon Cloud Clusters, Monthly Weather Review, 115, 505-519, 10.1175/1520-0493(1987)115<0505:Socowm>2.0.Co;2, 1987.

Wing, A. A. and Emanuel, K. A.: Physical mechanisms controlling self-aggregation of convection in idealized numerical modeling simulations, Journal of Advances in Modeling Earth Systems, 6, 59-74, 10.1002/2013ms000269, 2014.

Wing, A. A., Emanuel, K., Holloway, C. E., and Muller, C.: Convective Self-Aggregation in Numerical Simulations: A Review, Surveys in Geophysics, 38, 1173-1197, 10.1007/s10712-017-9408-4, 2017.

Yang, R., Zhang, Y., Sun, J., and Li, J.: The comparison of statistical features and synoptic circulations between the eastward-propagating and quasi-stationary MCSs during the warm season around the second-step terrain along the middle reaches of the Yangtze River, Science China Earth Sciences, 63, 1209-1222, 10.1007/s11430-018-9385-3, 2020.

Yuan, J. and Houze, R. A.: Global Variability of Mesoscale Convective System Anvil Structure from A-Train Satellite Data, Journal of Climate, 23, 5864-5888, 10.1175/2010jcli3671.1, 2010.

Yuan, J., Houze, R. A., and Heymsfield, A. J.: Vertical Structures of Anvil Clouds of Tropical Mesoscale Convective Systems Observed by CloudSat, Journal of the Atmospheric Sciences, 68, 1653-1674, 10.1175/2011jas3687.1, 2011.

Zhao, M.: An Investigation of the Connections among Convection, Clouds, and Climate Sensitivity in a Global Climate Model, Journal of Climate, 27, 1845-1862, 10.1175/jcli-d-13-00145.1, 2014.

Zhao, M., Golaz, J. C., Held, I. M., Ramaswamy, V., Lin, S. J., Ming, Y., Ginoux, P., Wyman, B., Donner, L. J., Paynter, D., and Guo, H.: Uncertainty in Model Climate Sensitivity Traced to Representations of Cumulus Precipitation Microphysics, Journal of Climate, 29, 543-560, 10.1175/jcli-d-15-0191.1, 2016.

Zhao, W., Marchand, R., and Fu, Q.: The diurnal cycle of clouds and precipitation at the ARM SGP site: Cloud radar observations and simulations from the multiscale modeling framework, Journal of Geophysical Research: Atmospheres, 122, 7519-7536, 10.1002/2016jd026353, 2017.

Zinner, T., Mannstein, H., and Tafferner, A.: Cb-TRAM: Tracking and monitoring severe convection from onset over rapid development to mature phase using multi-channel Meteosat-8 SEVIRI data, Meteorology and Atmospheric Physics, 101, 191-210, 10.1007/s00703-008-0290-y, 2008.

Zinner, T., Forster, C., de Coning, E., and Betz, H. D.: Validation of the Meteosat storm detection and nowcasting system Cb-TRAM with lightning network data – Europe and South Africa, Atmospheric Measurement Techniques, 6, 1567-1583, 10.5194/amt-6-1567-2013, 2013.